Chapter 3
Fiber Optic Imagers

Do-Hyun Kim and Jin U. Kang

3.1 Basic Fiber Optic Imager

In most fiber optic imagers, their main differences from their bulk optic imaging counterparts are that the free-space beam path and bulk optics components are replaced by optical fibers and fiber optic components. These seem to be relatively trivial differences; however, they greatly improve the functionality and practicality of the fiber optic imaging systems compared to bulk systems for a wide range of applications—especially for endoscopic, in situ imaging. An example of a simple fiber optic imager is shown in Fig. 3.1. It consists of a light source, a fiber coupler, a light detector, an imaging fiber, and an imaging probe. Depending on the applications, the fiber coupler can be a simple power splitter (normally a 50/50 power splitter), wavelength-division-multiplexing (WDM) coupler, or other type of wavelength- or polarization-dependent coupler.

The imaging fiber can be single-mode, multi-mode, or multi-core, also known as a fiber bundle. The imaging probe typically consists of either an optical lens, graded index lens, or ball lens.

D.-H. Kim (✉)
Center for Devices and Radiological Health, US Food and Drug Administration, 10903 New Hampshire Ave, Silver Spring, MD 20993, USA
e-mail: do-hyum.kim@fda.hhs.gov

J. U. Kang
Department of Electrical and Computer Engineering, Johns Hopkins University, 3400 N Charles Street, Baltimore, MD 21218, USA
e-mail: jkang@jhu.edu

J. U. Kang (ed.), *Fiber Optic Sensing and Imaging*,
DOI: 10.1007/978-1-4614-7482-1_3,

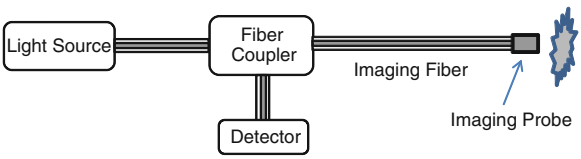

Fig. 3.1 Schematic of a simple fiber optic imager

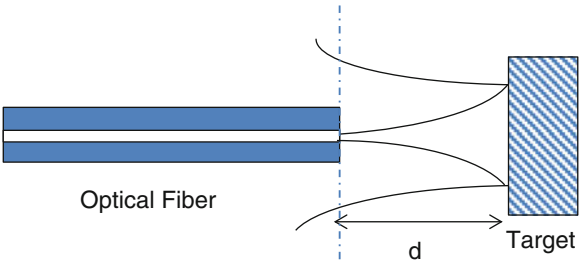

Fig. 3.2 Bare fiber probe

3.1.1 Simple Fiber Optic Imaging Probes: Single-Mode

The simplest imaging/sensing fiber optic probe is a bare fiber without any imaging components, as shown in Fig. 3.2. This is typically used when the working distance, d, is very small, less than a few hundred microns. In general, a Gaussian beam can be used to describe a beam profile exiting the optical fiber where it can be written as:

$$E(x, y, z) = E_0(z)e^{ik\frac{\rho^2}{2q(z)}} \tag{3.1}$$

where $\rho^2 = x^2 + y^2$, and the complex beam parameter, q, can be written in terms of the beam radius of curvature, R(z), and the beam width, w(z), as:

$$\frac{1}{q(z)} = \frac{1}{R(z)} - j\frac{\lambda}{\pi w^2(z)} \tag{3.2}$$

The Gaussian beam parameters can be analysed by a simple ABCD ray-transfer matrix where a new beam parameter, q_2, from the initial beam parameter, q_1, is related as:

$$q_2 = \frac{Aq_1 + B}{Cq_1 + D} \tag{3.3}$$

By combining Eqs. 3.2 and 3.3, one can derive the new beam width, w_2, as:

$$w_2^2 = \frac{B^2 + A^2\frac{\pi^2}{\lambda^2}w_0^4}{(AD - BC)(\frac{\pi^2}{\lambda^2}w_0^2)} \tag{3.4}$$

If we assume that the target is a perfect mirror, the overall ABCD matrix for beam propagation in free space for distance, d, reflected off of a target and propagating distance, d, back to the fiber can be written as:

$$\mathrm{M}_{Final} = \begin{bmatrix} A & B \\ C & D \end{bmatrix} = \mathrm{M}_{Return}\mathrm{M}_{FlatMirror}\mathrm{M}_{Incident} = \begin{bmatrix} 1 & \mathrm{d} \\ 0 & 1 \end{bmatrix}\begin{bmatrix} 1 & 0 \\ 0 & 1 \end{bmatrix}\begin{bmatrix} 1 & \mathrm{d} \\ 0 & 1 \end{bmatrix} = \begin{bmatrix} 1 & 2\mathrm{d} \\ 0 & 1 \end{bmatrix} \tag{3.5}$$

By combining 3.4 and 3.5, we can simplify Eq. 3.4 as:

$$w_2^2 = \frac{4d^2 + \frac{\pi^2}{\lambda^2} w_0^4}{\frac{\pi^2}{\lambda^2} w_0^2} \tag{3.6}$$

By defining the Rayleigh range or confocal parameter, z_0, as: $z_0 = \frac{\pi}{\lambda} w_0^2$ and the overall beam propagation distance, z, as z = 2d, the equation reduces to a well-known Gaussian beam width equation, which is in function of propagation distance as:

$$w_2^2 = w_0^2 \frac{z^2 + z_0^2}{z_0^2} \tag{3.7}$$

One of the main issues with the fiber probe is the coupling efficiency, T, of the returning beam back into the fiber. Due to the small aperture of the fiber, for a large z, the coupling efficiency is poor; this plays an important role in the quality of the images that can be obtained. The fiber coupling efficiency, T, assuming the system is lossless, can be calculated simply by an overlap integral between the fiber mode profile and the imaging beam profile. This can be written as:

$$T = \frac{\left| \iint F_r(x,y) W'(x,y) dxdy \right|^2}{\iint F_r(x,y) F_r'(x,y) dxdy \iint W(x,y) W'(x,y) dxdy} \tag{3.8}$$

where $F_r(x,y)$ is the imaging beam field profile at the distal end of the fiber as it returns back, and W(x,y) is the fiber mode field profile which is the beam profile of the imaging beam as it exits the fiber. From this model it is clear that the fiber does not "see" the full imaging beam as it returns back to the fiber. In general, the returning imaging field seen by the fiber, or W(x,y), is much larger than the beam diameter at the sample surface and the one exited from the fiber. Only when the target is in contact with the fiber end, the $F_r(x,y) = W(x,y)$ and T = 1 can be achieved, which describes the perfect coupling case. However, as z increases, $F_r(x,y)$ increases and this results in decreased coupling efficiency, T.

If a Gaussian beam profile is assumed, as in Eq. 3.1, the optical power collected by the fiber tip—which is the integral of the beam intensity over the fiber core area at the fiber tip plane—can be written as:

$$P_2 \propto \iint_s \frac{P_0}{w_2^2} \exp\left(-\frac{x^2+y^2}{w_2^2}\right) dxdy \propto \left[erf\left(\frac{r_0}{w_2}\right)\right]^2 \tag{3.9}$$

where P_0 is the power carried by the beam, s is the circular fiber core area with radius r_0, and $erf(u)$ is the error function defined as $erf(u) = \frac{2}{\sqrt{\pi}} \int_0^u e^{-t^2} dt$. For estimation it is assumed that $r_0 = w_0$. There T is calculated by dividing the right-hand side of Eq. (3.9) to $\left[erf\left(\frac{r_0}{w_0}\right)\right]^2$, which results in

$$T = \left[erf\left(\frac{r_0}{w_2}\right)\right]^2 / \left[erf\left(\frac{r_0}{w_0}\right)\right]^2 = \left[erf\left(\frac{w_0}{w_2}\right)\right]^2 / \left[erf(1)\right]^2 \tag{3.10}$$

The result above shows that the working distance for the bare fiber probe is less than 0.5 mm. However, this also means that the bare fiber probe works very well, better than the ones with lensed imagers if the working distance is less than 0.1 mm, with the best image occurring when the probe is in contact with the target, i.e., z = 0 (Fig. 3.3).

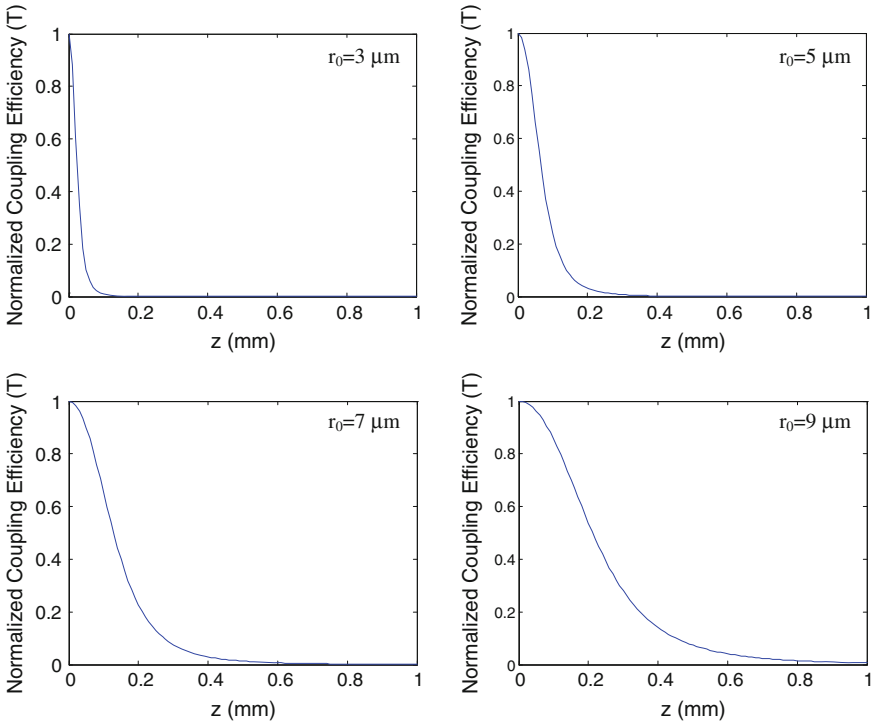

Fig. 3.3 Normalized coupling efficiency of a simple fiber probe as a function of total propagation distance, z, which is twice the target distance for 4 different fibers with varying core radius, r_0

3.1.2 Simple Fiber Probe Transverse Resolution

For all imaging systems, it is automatically assumed that the resolution of the imaging system is limited by the beam spot size. Even for a bare fiber probe, as shown in Fig. 3.2, it is often assumed that the resolution follows the Gaussian beam propagation where the beam width changes as (rewriting 3.7):

$$w_2(z) = w_0\left(1 + \frac{z^2}{z_0^2}\right)^{1/2} \tag{3.11}$$

Rayleigh range, z_0, is defined as the distance at which the beam width increases by $\sim$1.4 times the original beam width. However, the lack of imaging system makes the bare fiber probe-based imaging system non-reciprocal and the finite aperture size of the fiber affects the effective resolution of the probe. In other words, the resolution of such imaging system is limited by the imaging beam coupling back to the fiber.

3.1.2.1 Resolution Measurement

To measure the resolution of the bare fiber imaging probe, one can use a simple test setup shown in Fig. 3.4. This particular experiment was performed using an 800 nm source and a fiber having a core diameter of $\sim$5 microns. It measures the received signal power as the fiber probe is scanned across a United States Air Force (USAF) target containing high/low reflectivity boundary at some height above the target.

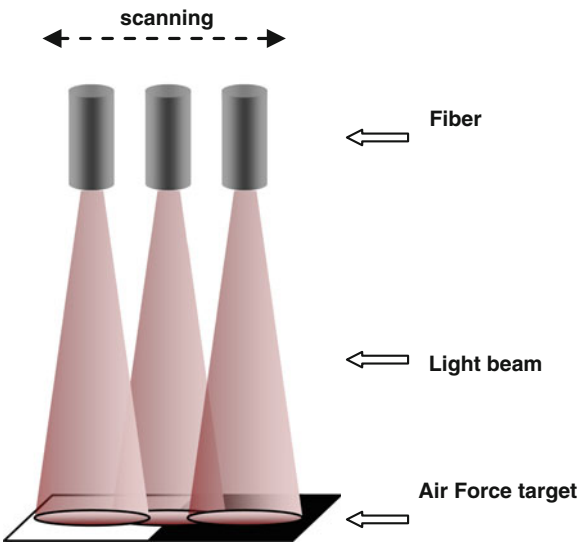

Fig. 3.4 Experimental setup to measure the transverse resolution of a fiber probe

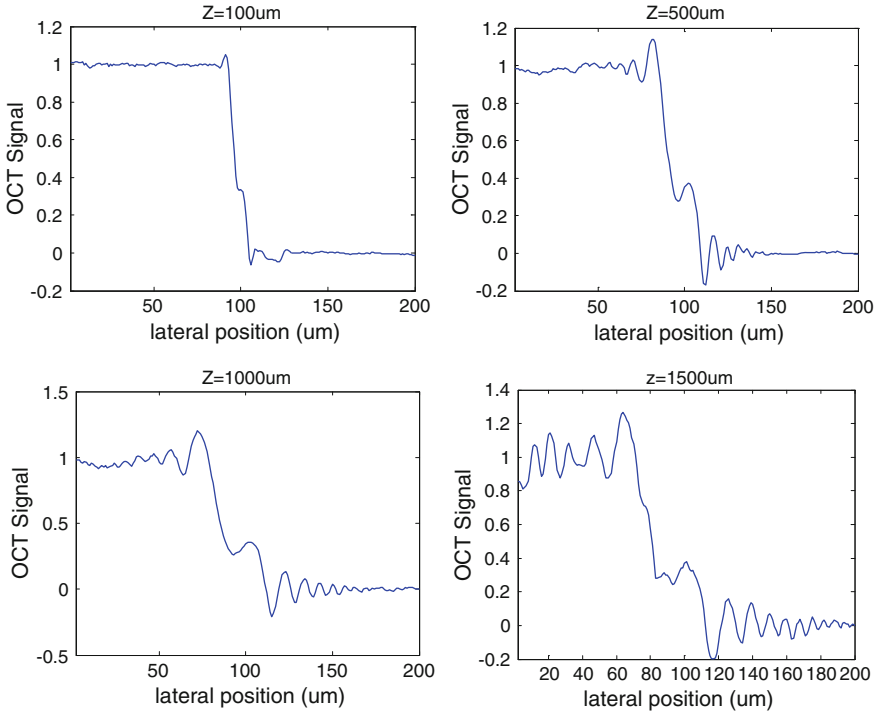

Fig. 3.5 Experimentally obtained, normalized signal for 4 different imaging distances between the fiber probe and the target, showing the transverse response function of the probe for a target having a sharp boundary at the lateral position of $\sim$100 microns

The test result is shown in Fig. 3.5 for 4 different imaging distances between the fiber probe and the target. The sharpness of the signal falling edge as the fiber is scanned from the high reflection to low indicates the resolution of the system. As can be seen from the figures, as z increases, the resolution of the bare fiber imaging system degrades. The ringing is the result of the edge diffraction.

The experimental result in Fig. 3.5 can be simulated using the signal coupling efficiency described by Eq. 3.8. The simulation result is shown in Fig. 3.6. From both the experimental and theoretical results, it can be clearly seen that the sharpness of the edge decreases significantly as the z increases. Again, the ringing around the edges is due to the edge diffraction, which will not be discussed in this book.

From these results, the system point-spread function **(PSF),** $p(x)$ of the bare fiber probe imaging system to an impulse input, $\delta(x)$, can be obtained. Since the input used in both the simulation and experiment is a step function, $u(x)$, the output of the system, $f(x)$, can be expressed as:

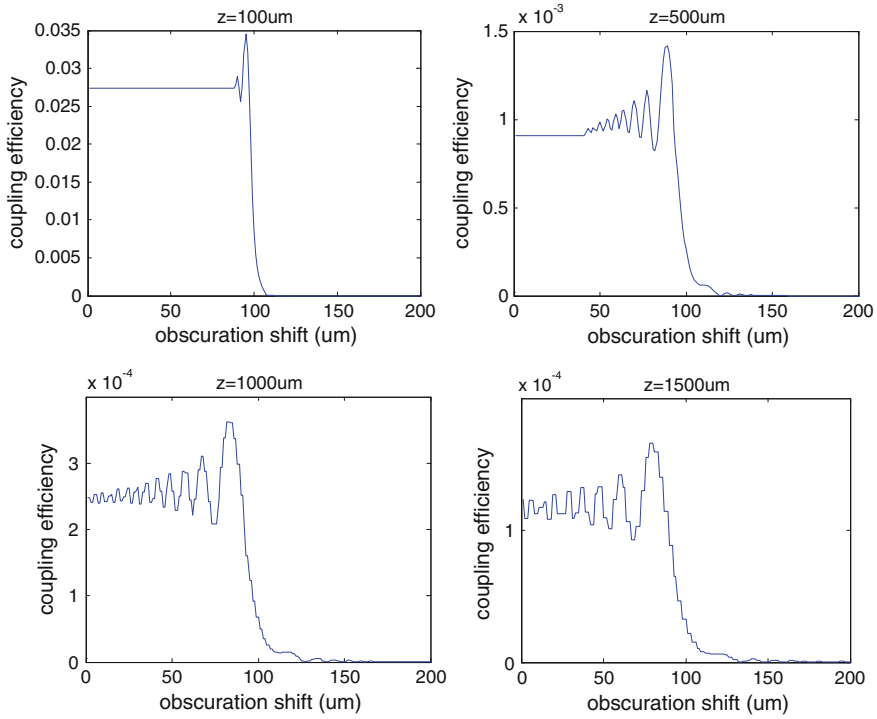

Fig. 3.6 Numerically calculated, normalized signal for 4 different imaging distances between the fiber probe and the target showing the transverse response function of the probe for a target having a sharp boundary at the lateral position of $\sim$100 microns

$$f(x) = p(x) \otimes u(x) = \int_{-\infty}^{+\infty} p(x')u(x - x')dx' \tag{3.12}$$

By taking the derivative of both sides, we can obtain an expression for the PSF as:

$$\frac{df(x)}{dx} = \int_{-\infty}^{+\infty} p(x') \frac{d[u(x - x')]}{dx} dx' = \int_{-\infty}^{+\infty} p(x')\delta(x - x')dx' = p(x) \tag{3.13}$$

Here the full-width half-maximum (FWHM) of the PSF is defined as the lateral resolution. Again we assumed the beam profile to be Gaussian, $f(x)$ and the corresponding error function is written as:

$$f(x) = A_0 \int_x^{\infty} \exp(-ax^2)\, dx = B_0 erfc(-bx) \tag{3.14}$$

The function, *erfc,* is called the complementary error function.

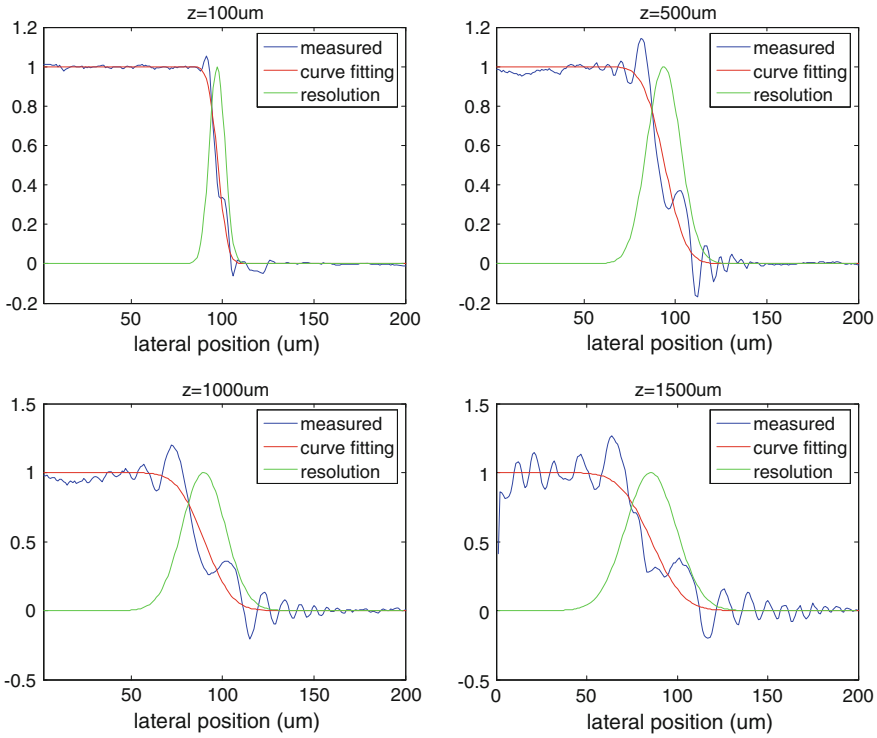

Fig. 3.7 Calculated PSF for 4 different imaging distances between the fiber probe and the target by fitting the experimental data obtained in Fig. 3.5

Using the experimental graphs in Fig. 3.5, the corresponding PSF can be extracted and Fig. 3.7 shows the PSF, or the resolution of the system for 4 different values of z. Clearly, PSF broadens with the increasing z.

Again using the theoretical graphs in Fig. 3.6, the corresponding PSF can be extracted and Fig. 3.8 shows the theoretical PSF result.

The resolution result is summarized in Fig. 3.9, where the transverse resolution obtained from both experimental and simulation results are plotted as a function of imaging distance. Note that the transverse resolution of the bare fiber probe is much better than that deduced by the spot size of the beam. For example, even when the target surface is 1.5 mm away from the end of the fiber probe, the resolution is still a respectable $\sim$33 um. In comparison, the beam size at the target is approximately 75 microns. To obtain <10 um resolution, the imaging distance has to be <100 um.

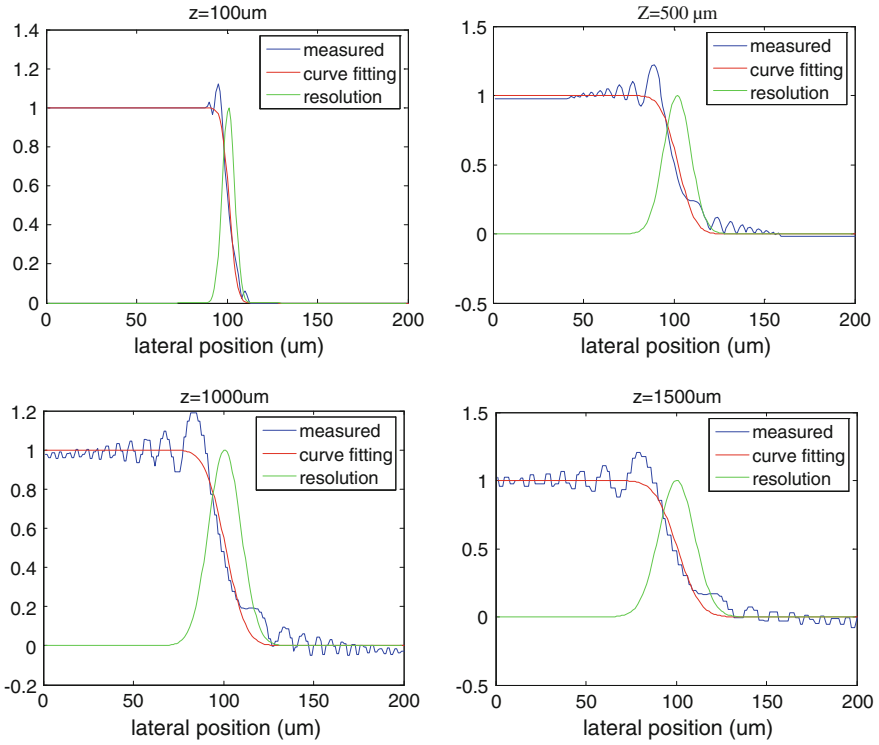

Fig. 3.8 Calculated PSF for 4 different imaging distances between the fiber probe and the target by fitting the calculated data obtained in Fig. 3.6

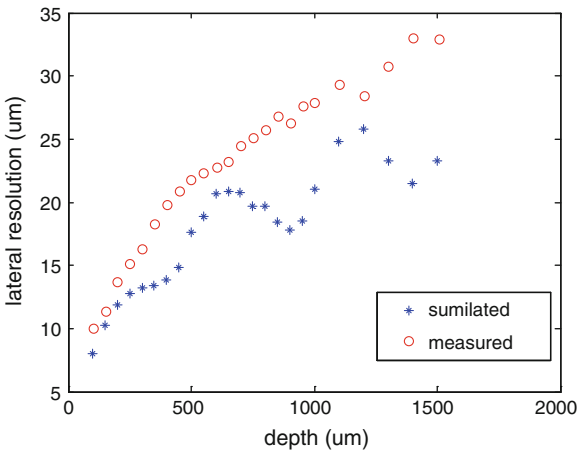

Fig. 3.9 Transverse (lateral) resolution of a bare fiber probe as a function of target depth

3.1.3 Simple Fiber Probe with Thin Lens

A fiber optic imager that requires a longer working distance >0.5 mm requires a lens to form an image at the distal end of the fiber, as shown in Fig. 3.10.

Following the same procedures shown in Sect. 3.1.1., the total ray-transfer matrix can be written as:

$$\begin{aligned} M_{Final} &= M_{Return} M_{FlatMirror} M_{Incident} \\ &= \begin{bmatrix} 1 & d_1 \\ 0 & 0 \end{bmatrix} \begin{bmatrix} 1 & 0 \\ -\frac{1}{f} & 1 \end{bmatrix} \begin{bmatrix} 1 & d_2 \\ 0 & 1 \end{bmatrix} \begin{bmatrix} 1 & 0 \\ 0 & 1 \end{bmatrix} \begin{bmatrix} 1 & d_2 \\ 0 & 1 \end{bmatrix} \begin{bmatrix} 1 & 0 \\ -\frac{1}{f} & 0 \end{bmatrix} \begin{bmatrix} 1 & d_1 \\ 0 & 1 \end{bmatrix} \end{aligned} \tag{3.15}$$

If the distance from the fiber to the lens, d_1, is set to 2f, i.e., $d_1 = 2f$, the equation reduces to:

$$M_{Final} = \begin{bmatrix} A & B \\ C & D \end{bmatrix} = \begin{bmatrix} \frac{2d_2}{f} - 3 & 2d_2 - 4f \\ -\frac{2}{f} + \frac{2d_2}{f^2} & \frac{2d_2}{f} - 3 \end{bmatrix} \tag{3.16}$$

By combining 3.4 and 3.16, we can simplify the Eq. 3.4 as:

$$w_2^2 = \frac{4(d_2 - 2f)^2 + (\frac{2d_2}{f} - 3)^2 \frac{\pi^2}{\lambda^2} w_0^4}{\frac{\pi^2}{\lambda^2} w_0^2} \tag{3.17}$$

The result above shows that the imaging depth is critically dependent on the size of the fiber mode. This effect is expected from the well-known confocal imaging where the depth resolution depends on the size of the aperture used. The detail of this effect and the fiber confocal imager is reviewed in detail in Sect. 3.2 (Fig. 3.11).

3.2 Fiber Optic Confocal Microscope

3.2.1 Review of Fundamentals of Microscope

A fiber optic confocal microscope (FOCM) is a type of confocal microscope in which the confocal pinhole is replaced by an optical fiber. Fundamentals of wide-field and conventional confocal microscopy apply to an FOCM, some of which

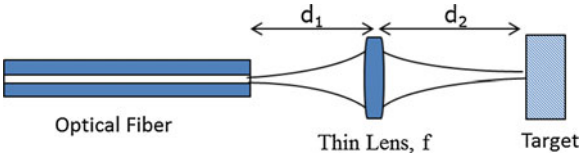

Fig. 3.10 Simple fiber probe with a thin lens having a focal length, f

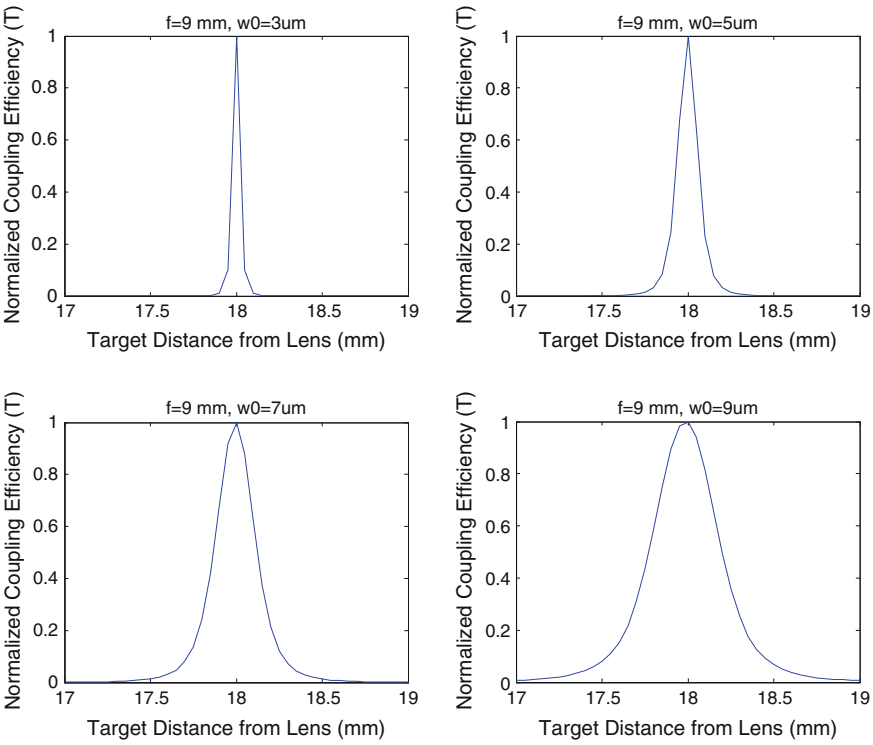

Fig. 3.11 Normalized coupling efficiency as a function of target distance from lens, d_2, for a simple fiber probe with a thin lens

will be introduced in this section briefly. More details of wide-field microscopy and confocal microscopy can be found in other books, for example, Mertz's [1] and Pawley's [2]. The principal goal of microscopy is to enlarge images to a certain extent, so that they can reveal details of objects not perceived by the unaided eye. The ability of a microscope to reveal details, in a more scientific way of description, is defined by the resolving power, which is an instrument property, specifying the smallest detail that a microscope can resolve in imaging an ideal specimen [3]. The related quantity—resolution—refers to the detail actually revealed in the image of a given specimen. Although resolving power refers to a property of the instrument and resolution refers to the level of detail obtained in the resulting image, both are quantified in terms of minimum resolvable distance, $d_{\min}$.

Ernst Abbé described the existence of a resolution limit in 1873 using the diffraction theory, which is now commonly known as Fourier optics. The key idea of Fourier optics is that the image formed from the specimen through an optical system is the superposition of diffracted images of each point of the specimen, and the image of the point itself is its Fourier transform–an Airy disk.

The size of the Airy-disk and its higher-order surrounding diffraction rings limit the highest resolution possible. There are many different ways to define the minimum resolvable separation. The most commonly adapted definition is the Rayleigh criterion: two overlapping Airy-disk images are resolvable when the central maximum of one coincides with the first minimum of the other (see Fig. 3.12a).

For quantitative analysis purposes, the image of a point observed through an optical system is expressed as the point-spread function (PSF). Image obtained by an optical system is a superposition of PSF of an extended object. The intensity PSF is related to both lateral and axial resolution of a microscope. The amplitude PSF can be calculated through a somewhat complicated procedure which can be found in many optics text books (for example, [4]), and is expressed as:

$$h(u,v) = -i\frac{2\pi nA\sin^2\alpha}{\lambda}e^{iu/\sin^2\alpha}\int_0^1 J_0(v\rho)e^{iu\rho^2/2}\rho d\rho \tag{3.18}$$

where λ is the vacuum wavelength, n is the refractive index, $n\sin\alpha$ is the numerical aperture of the lens, A is the area of the illumination, J_0 is the zeroth-order Bessel function. When the light path is in the z direction, v and u are normalized optical units perpendicular and parallel to z, respectively:

$$v = \frac{2\pi nr\sin\alpha}{\lambda} \tag{3.19}$$

$$u = \frac{2\pi nz\sin^2\alpha}{\lambda} \tag{3.20}$$

where, $r = \sqrt{x^2+y^2}$. The intensity PSF is given by $|h(u,v)|^2$.

As mentioned earlier, one way to define the resolution is to use the Rayleigh criterion. In this case, as can be seen in Fig. 3.12a, the resolution corresponds to

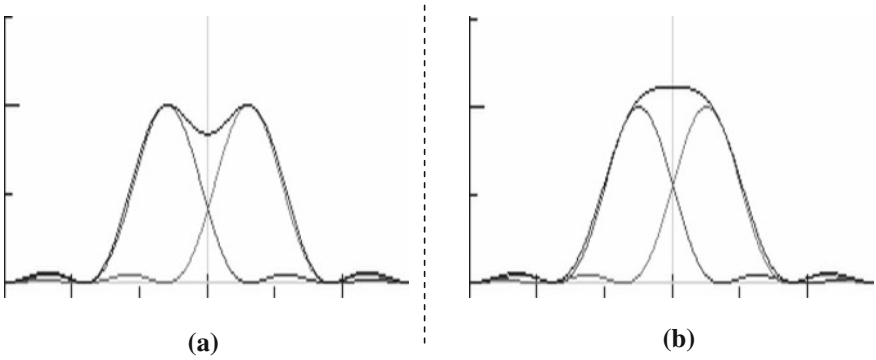

Fig. 3.12 Superposition of Airy disks. **a** Central maximum of one Airy disk coincides with the first minimum of the other. **b** Separation between two Airy disks are minimal to give non-zero superposition

the separation at which a 26 % contrast is achieved. Another commonly used way to define resolution is the separation at which the contrast is non-zero, any value between 0 and 100 % (see Fig. 3.12b). The Rayleigh criterion will be adapted throughout this section.

Under the Rayleigh criterion, we can define the lateral resolution for a conventional microscope as the distance between the central maximum and first minimum of the Airy disk, which is given by:

$$r_{xy} \approx \frac{1.22\lambda}{2NA} = \frac{0.6\lambda}{NA} \tag{3.21}$$

$$r_z \approx \frac{2\lambda n}{NA^2} \tag{3.22}$$

where λ is the wavelength of the light source and NA is the numerical aperture of the objective lens. This equation is convenient for calculating the lateral resolution of a conventional wide-field microscope, at which a reasonable contrast is obtained. In practice, it is difficult to measure the location of an intensity minimum; hence, it is quite common to measure the full-width at half-maximum (FWHM) of the microscope's PSF to determine the resolution experimentally. The measured value of FWHM is approximately 17 % smaller than the calculated value of r_{xy}.

3.2.2 Laser Scanning Confocal Microscopy (LSCM)

The word confocal means "of-same-foci." Confocal microscopy is different from wide-field microscopy because it restricts the detection of signals from the object by using a confocal aperture placed in front of the detector and on the conjugate plane of the image. Another aperture may be placed in front of the illuminator to increase spatial coherency and thus to produce a diffraction-limited illumination spot on the sample; however, this is not completely necessary. This is illustrated in Fig. 3.13.

In a scanning microscope, the illumination and/or focused image is confined to a very small region, usually a diffraction-limited spot; thus, scanning of small spots over the larger specimen area is necessary to reconstruct a usable image containing a region of interest larger than a diffraction-limited spot; hence, the name scanning microscope.

The advantage of a confocal microscope is prominent when a thick sample is being imaged. The sample must be thicker than the depth of field of the objective lens. Figure 3.13a illustrates wide-field illumination combined with wide-field imaging. The entire sample is illuminated and the signal—either scattered light or fluorescence emission from the sample—is projected onto the image plane with a certain thickness. Since the image is recorded by the detector, such as a focal plane array placed at the image plane, the light signal from a thick sample will contribute

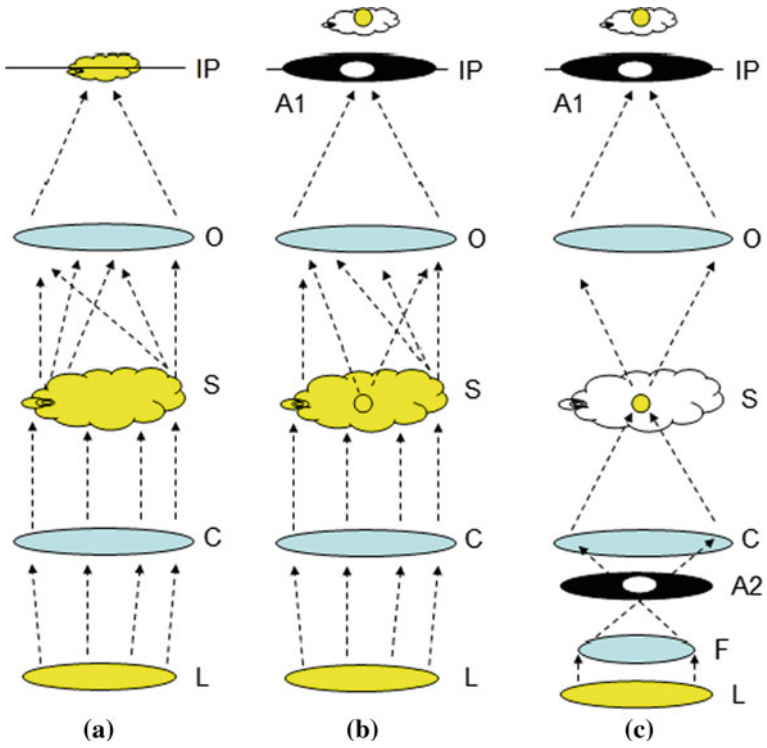

Fig. 3.13 (**a**) Illustration of a wide-field illuminating and wide-field imaging microscope; (**b**) wide-field illuminating and confocal imaging microscope; (**c**) point-illuminating and confocal-imaging microscope. *L* lamp, *C* condenser, *S* sample, *O* objective lens, *IP* image plane, *F* focusing lens, *A1* aperture at the image plane, *A2* aperture at the back-focal-plane of the condenser

to the recorded image in forms of blurriness or decreased contrast. If a confocal aperture is placed in front of the detector, as shown in Fig. 3.13b, then majority of the signal from the conjugate spot in the sample will be projected onto the aperture (thus confocal). Lights scattered or fluoresced from the spot other than the confocal spot will be rejected. The detector does not have to be a focal plane array, thus it can be replaced by a highly efficient photo-multiplier tube (PMT). When the sample or the aperture is raster scanned along the image plane (IP), a two-dimensional (2D) image of the sample only from the conjugate plane of IP is reconstructed. Although the arrangement shown in Fig. 3.13b, which is wide-field illumination combined with confocal detection, represents confocal microscopy, it does not utilize the illuminating power of the light source (L) entirely. As a matter of fact, this illumination scheme is highly inefficient because all the lights are lost except that which illuminates a very small spot in the sample. The arrangement shown in Fig. 3.13c solves this problem by using point illumination and point confocal detection, which is most common in modern confocal microscopy. It also

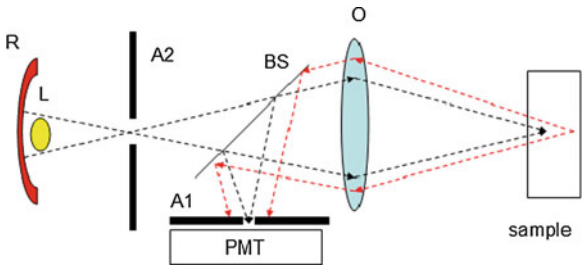

Fig. 3.14 Illustration of an epi-illumination confocal microscope. *R* focused reflector, *L* lamp, *O* objective lens, *A1* detector aperture, *A2* illuminator aperture, *BS* beam-splitter

provides higher rejection of scattered lights compared to Fig. 3.13b. An epi-illumination version of Fig. 3.13 leads to the famous illustration from Minsky's original invention report of confocal microscopy [5], which is shown in Fig. 3.14.

The advantage of epi-illumination is that one lens can play the role of condenser as well as that of objective lens. However, not all types of samples produce a decent epi-illuminated signal; thus, epi- or trans-illumination must be chosen carefully depending on the sample type. As can be seen in Fig. 3.14, the signal from the sample other than the focal spot is rejected by the aperture in front of the detector (A1). If the beam-splitter is replaced by a dichroic mirror that splits the excitation wavelength and emission wavelength, then the confocal microscope shown in Fig. 3.14 runs as a fluorescence confocal microscope.

For confocal microscopy, the FWHM extent of both lateral (xy-plane) and axial (z-direction) PSF are about 30 % narrower than that of a conventional wide-field microscope [6]. This improved PSF can be explained by Lukosz's principle [7]. The improvement is due to the rejection of scattered light from out-of-focus which contributes to the improvement of contrast. As was mentioned in Sect. 3.2.1, the resolving power of the optical system is determined by the optical elements (mostly by lenses), thus it remains the same for a wide-field microscope and confocal microscope when the same lenses are used. Resolution is the result induced from both resolving power and contrast; thus, resolution of a confocal microscope is slightly higher than that of a wide-field microscope, which is quantified as 30 % from experimental measurements and mathematical calculations [6].

$$r_{xy,confocal} \approx \frac{0.4\lambda}{NA} \tag{3.23}$$

For point-like objects, the same approach can be applied to determine a microscope's axial resolution. As in the lateral direction, the same Rayleigh criterion can be applied, resulting in:

$$r_{z,confocal} \approx \frac{1.4\lambda n}{NA^2} \tag{3.24}$$

Here, n stands for the refractive index of the specimen. As n is normally larger than 1 and NA is smaller than 1, the axial resolution is poorer than the lateral resolution. Practically, there are several technical concerns which reduce the

resolution of the system: the size of the pinhole and pixilation of the confocal microscope, noise of the detector, and the precision of the focusing mechanism.

Note that placing a pinhole with an arbitrary diameter will not guarantee the confocal operation of the system. If a pinhole is large enough that all the incoming signals—including that from the scattered light—pass through the pinhole, then the pinhole does not play any role; the system is simply a wide-field microscope with a limited field of view. Also, if a pinhole is too small, then the signal level will be too low to acquire optimal image quality. Diffraction from the pinhole will also affect the image quality negatively. Wilson et al. [8] showed that optimal confocality of the system is achieved when the optical coordinate v of Eq. 3.19 is less than 0.5.

$$v = \frac{2\pi n r \sin\alpha}{\lambda} < 0.5 \tag{3.25}$$

This can be rewritten as:

$$r < \frac{\lambda}{4\pi n \sin\alpha} \tag{3.26}$$

For example, when a 40 × NA 0.6 numerical aperture objective lens is used in the setup shown in Fig. 3.14, the diameter of the pinhole needs to be 6.7 μm or less for the system to be operated in a confocal mode with 632.8 nm He–Ne laser in air (n = 1). The smaller the pinhole diameter is, the higher the confocality of the system becomes; however, due to the signal loss, the pinhole does not have to be practically smaller than 6.7 μm. Improvement in resolution by using a pinhole smaller than 6.7 μm is also negligible.

3.2.3 Laser Scanning Confocal Microscope

A laser scanning confocal microscope (LSCM) is widely used; however, there are other types such as a spinning (Nipkow) disk confocal microscope [9] and a programmable array microscope [10]. A fiber-optic confocal microscope (FOCM) is a type of LSCM, thus only LSCM is considered in this chapter. Compared to other confocal microscopes, LSCM is unique because it uses a laser as the light source and the laser is scanned, not the sample or the detector. As mentioned previously, using laser as a light source enables achieving a diffraction-limited focal spot due to the high spatial coherence of laser. However, high coherence sometimes decreases the image quality of LSCM when interference is formed between the slide cover and objective lens. Scanning the sample—or sometimes, the detector—gives the highest image quality without the spherical aberrations induced in laser scanning. However, scanning the laser almost always achieves the highest scanning speed, thus the highest image acquisition rate. A typical LSCM setup is shown in Fig. 3.15.

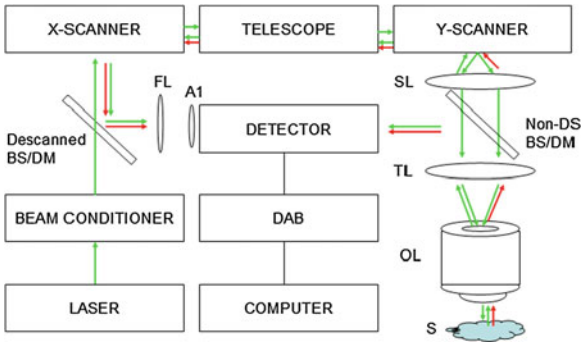

Fig. 3.15 Schematic of a typical LSCM. *BS* beam-splitter, *DM* dichroic mirror, *SL* scanning lens, *TL* tube lens, *OL* objective lens, *S* sample, *DAB* data acquisition board, *FL* focusing lens, *A1* confocal aperture

The example shown in Fig. 3.15 uses green (532 nm) laser as the light source. The beam conditioner usually contains a power adjustment element such as a variable neutral density filter or Pockel's cell, beam expander, laser shutter, polarizer, laser power monitor, spatial filter, regenerative amplifier, etc. Any of these components can be omitted if necessary. Beam-splitters are in general 50:50 splitters, and can be replaced by dichroic mirrors for fluorescence-mode operation. The X-scanner is in general a fast-scanner and can be a mirror scanned by galvo-motor, resonant-motor, or rotating mirror block. The Y-scanner is a slow-scanner, and a galvo-motor is commonly used. An acousto-optic tunable filter can also deflect the laser beam, and thus is used as the fast-scanner. A telescope between the X- and Y-scanners is not always necessary; however, it helps to reduce comma-errors in scanning by placing the pivotal point of the scanning mirrors at the back-focal plane of the scanning lens. When a telescope is not used, the X- and Y-scanners should be placed as close as possible. The relationship between SL, TL, and OL will be explained in more detail.

If the reflected light or fluorescence emission is captured by the detector using a non-descanned (DS) beam-splitter or dichroic mirror, the microscope is being operated under non-descanned mode. This is the common arrangement in two-photon microscopes. The microscope is not a confocal microscope, although it is still a laser scanning microscope. For this type of arrangement to be operated under a confocal regime, the signal must be collected using the descanned BS or DM, and the detector must be accompanied by the focusing lens (FL) and the aperture placed at the focal plane of the FL. IF FL and A1 are removed, the setup is no longer a confocal microscope, even though the signal is descanned. Descanned detection without a confocal aperture is almost meaningless, except that the illumination laser intensity can be higher than a wide-field microscope. Non-descanned confocal operation is impossible because the pinhole position cannot be fixed for a non-descanned (thus, still scanning) beam.

Figure 3.16 shows fluorescence microscopy images obtained by using both a wide-field fluorescence microscope and LSCM. The sample was a prepared test slide from Invitrogen (#F-24630), which is a mouse kidney section stained with Alexa Fluor 488 WGA, Alexa Fluor 568 Phalloidin, and DAPI. Figure 3.16a is a

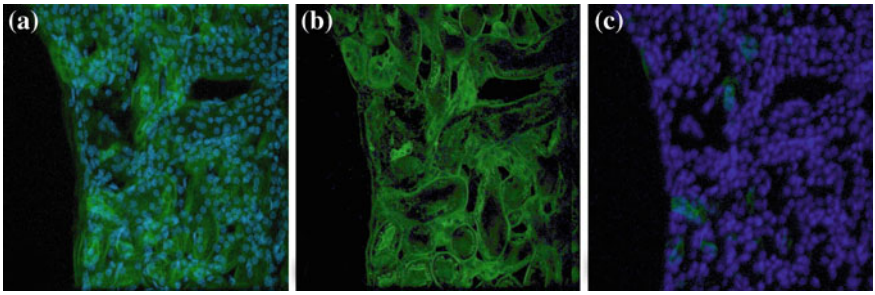

Fig. 3.16 (**a**) Wide-field fluorescence image; (**b**) Confocal fluorescence image from channel 1; and (**c**) channel 2. See text for more detail

wide-field image with 405 nm excitation. Emissions from both Alexa Fluor 488 (shown in green in the figure) and Alexa Fluor 568 (shown in blue in the figure) can be seen in one image. Figure 3.16b and c are confocal fluorescence images using 405 nm excitation and two PMT channels separated by a dichroic filter: Channel 1 is for >505 nm and Channel 2 is for <505 nm. Both channels are overlaid in Fig. 3.16b and c. The difference between Fig. 3.16b and c is their sample z-position. The depth discrimination capability of confocal microscopy can be clearly seen in both figures. At different depths—not like the wide-field image shown in Fig. 3.16a—only one emission can be dominantly seen in Fig. 3.16b and c. Cells and organelles in kidney are stained by different dyes, thus their depth positions in z-direction are separated by different emissions. Also, Fig. 3.16b and c demonstrate sharper boundaries compared to Fig. 3.16a, which is enhanced by rejection of scattered light. Depth discrimination and rejection of scattered light (thus a slightly higher resolution) are two major advantages of confocal microscopy over wide-field microscopy. Optical arrangement of scanning lens, tube lens, and objective lens is critical for successful operation of LSCM in confocal mode, along with achieving high confocality of the system.

Objective lenses are designed so that their highest diffraction-limited resolution is achieved when their back apertures are filled with collimated monochromatic light. Since the incoming light fills the back aperture of OL, scanning can be achieved only by changing the incident angle (θ) of the incoming light relative to the optical axis of OL, which is illustrated in Fig. 3.17a. Each OL has the maximum allowable incident angle (θ_{max}) which produces a usable image of the sample with minimal spherical aberration. Any incoming light with an incident angle larger than θ_{max} will result in a distorted or unevenly illuminated image. The back-aperture size of commonly used OL varies greatly: for example, Zeiss W Plan-APO 20x/1.0NA lens which is widely used for in vivo imaging has a back aperture with 18.0 mm diameter while Zeiss W Plan-APO 60x/1.0NA lens has a 6.0 mm aperture. Lasers usually produce a collimated Gaussian output beam with a diameter of 1.0–2.0 mm. Thus, SL and TL must provide a proper incident angle (θ) with a properly expanded beam diameter to OL. The less the SL-TL pair expands the laser beam, the less the distortion from the scanning; however,

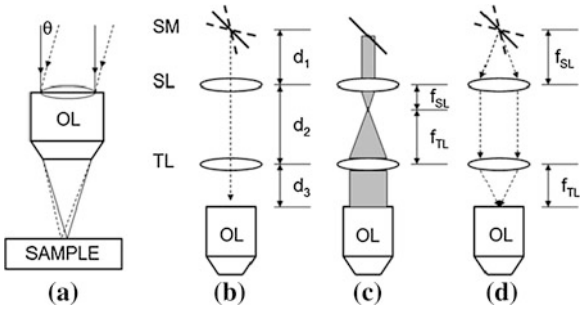

Fig. 3.17 (**a**) Illustration of the incident angle of an incoming scanning beam that fills the back aperture of an objective lens (*OL*); (**b**) Illustration showing the relative distance between scanning mirror (*SM*), scanning lens (*SL*), and tube lens (*TL*); (**c**) Illustration showing the function of SL and TL which expands the incoming collimating beam to fill the back aperture of the objective lens (*OL*). The sum of the focal lengths of SL (f_{SL}) and TL (f_{TL}) equals d_2; (**d**) Distance between the pivotal points of SM and SL needs to be f_{SL}, and distance between TL and back aperture of OL needs to be f_{TL}

scanning mirrors are limited for their sizes because their scanning speed is limited by the inertia of the mirrors. The role of beam expansion by an SL-TL pair is inevitable.

Figure 3.17b–d show the relative distances between SM, SL, and TL that are required for the optics to achieve proper beam expansion and scanning. Optimal performance of the scanning system critically depends on this optical arrangement. Focal lengths of SL (f_{SL}) and TL (f_{TL}) are chosen so that the pair provides the necessary beam expansion, as shown in Fig. 3.17c. For example, if the input beam diameter is 3 mm and the back aperture of OL is 6 mm, the SL-TL pair must provide 2-fold beam expansion; thus, $f_{TL}/f_{SL} = 2$ and $d_2 = f_{SL} + f_{TL}$. For the scanning system to achieve the most uniform illumination while providing incident angle to OL as large as θ_{max}, the distance between SL and the pivotal axis of SM needs to be f_{SL} ($= d_1$). Also, for the scanning beam to pass through the back aperture of OL with minimal translational shift, the distance between TL and the back aperture plane of OL needs to be f_{TL} ($= d_3$).

Measurement of the enhanced lateral (xy-plane) resolution of a confocal microscope is difficult, because there is no standardized resolution test-target that simulates a thick scattering biological specimen. If a generic USAF 1951 resolution target is used, the enhancement in lateral resolution may not be clearly detected; however, enhancement of axial (z-axis) resolution can be measured relatively easily. A simple method to measure the axial response is to scan a perfect reflector axially through its focus and measure the signal strength. Figure 3.18 shows a typical response.

A confocal system with less than an optimal optical arrangement will demonstrate a highly asymmetrical or Gaussian axial response. Practically, achieving perfect axial response, as shown in Fig. 3.18, is highly challenging. Asymmetry is

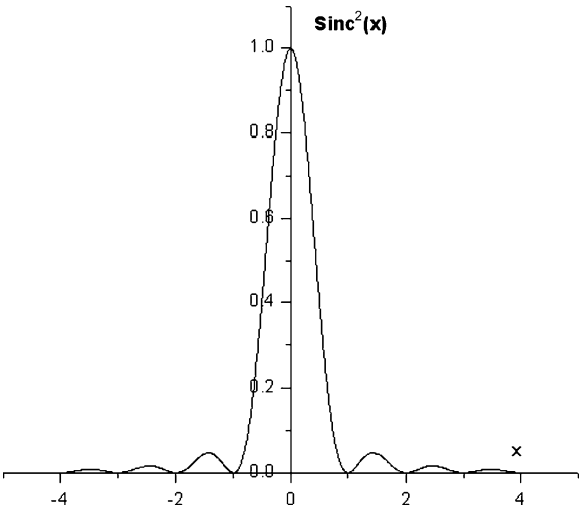

Fig. 3.18 A typical axial response of a confocal microscope–a squared Sinc function

hard to remove completely due to the optical design of the objective lens itself (mainly due to spherical aberration); however, it should be minimized. Other factors depending on the mirror defocus, such as system magnification, effective numerical aperture, and axial position also contribute to the asymmetric axial response.

3.2.4 Introduction to Fiber-Optic Confocal Microscopy

Due to their flexibility and robustness, optical fibers enable delivery of lights to hard-to-reach places as well as to collect them. Optical fibers also enable the separation of the optical components such as the light source and detectors from each other. Optical fibers have been adapted in confocal microscopy since the early 1990s [11] and can be found in many commercial wide-field microscope systems and endoscopic microscopy (endo-microscopy) systems. However, flexibility and robustness are not the only factors that make optical fibers unique in confocal microscopy applications. There are strong advantages of using optical fibers in confocal microscopy, including the following:

1. The output from a small-core single-mode fiber serves as an ideal Gaussian point-like light source, which contributes to achieving the diffraction-limited focal spot of the objective lens, thus achieving the highest possible resolution from given optics. This advantage is especially useful when a cost-effective diode laser is the light source, which does not have a Gaussian profile. However, this advantage is not very useful when a laser system with TEM_{00} mode output is available.

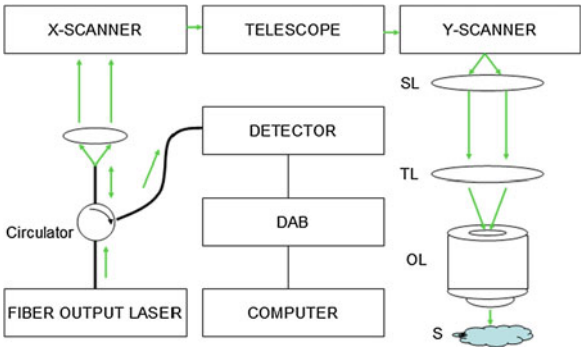

Fig. 3.19 Schematics of FOCM. Single-mode fiber tip serves as the point light source as well as the pinhole detector. Adaptation of an all-fiber circulator enables the entire construction to be simple and robust. Scanning and microscopic optics remain the same as the bulk optics version of Fig. 3.15

2. The core of an optical fiber is an ideal pinhole, in terms of shape and size. As described in Sect. 3.2.2, the pinhole diameter required for a NA = 0.6 lens with 632.8 nm laser in air is a few μm. A conventional pinhole with this size is very hard to produce: the shape of the pinhole can be irregular or the size can be incorrect. However, typical single-mode fibers have cores with a diameter in the order of a few μm. Once the signal is coupled into the detecting fiber, its delivery of light to the detector can be arranged in various ways so that the light collection efficiency can be maximized.
3. One of the disadvantages of using optical fiber as the pinhole is reduced collection efficiency. To efficiently couple the light into an optical fiber, not only the size of the focused signal light needs to be matched to the fiber core, but also the light field and numerical aperture must match those of the optical fiber. Adjusting the field and numerical aperture of signal light is almost impossible when the signal is a low-coherent fluorescence from biological samples. Also, since biological samples exhibit various levels of signal—whether it be fluorescence or reflectance—sometimes the size of the pinhole needs to be enlarged at the expense of reduced confocality. Many commercial confocal microscopes adapt multi-mode fiber with core size as large as 600 μm accompanied by a variable pinhole placed in front of the fiber tip. More details about collection efficiency will be discussed in a following section.
4. An all-fiber coupler or circulator makes it possible to use the fiber as the output source as well as the input source at the same time. This arrangement, as shown in Fig. 3.19, might be the best application of optical fibers in confocal microscopy in terms of utilizing the advantages of optical fiber over pinholes. One technical difficulty in such implementation stems from the fact that both ends of the fiber are in the image planes of the microscope. As a result, Fresnel reflection of the incident laser at the fiber tip can reduce the signal level. Careful management of reflections at the optical surfaces using angled fiber tips, anti-reflection coatings, and index-matching fluids helps reduce this unwanted effect [2].
5. Use of a miniature lens (such as a graded-index lens) attached to the tip of the optical fiber enables significant reduction of the optics size.

3.2.4.1 Coherent Detection

Once collimated using a collimating lens, the laser output from an optical fiber is no different than that from solid-state or gas lasers. Optical fiber as the light source in FOCM does not affect image characteristics due to the characteristics of the fiber. However, there is a significant difference between pinhole and optical fiber as detectors because optical fiber acts as a coherent detector. Single- and multi-mode fibers both serve as coherent detectors. Also, the spatial distribution of modes within a multi-mode detection fiber may also carry information regarding the source of the signal [2]. Not only does the size of the core of the optical fiber affect the confocality and signal level as the pinhole does, but also the mode of the incoming signal and the numerical aperture of the coupling lens affect the overall performance. For a pinhole, the signal is integrated over the area of the pinhole, while the signal is integrated over the modes at the entrance of the fiber. Since axial response is more affected by the coherent detection, the axial response of FOCM will be discussed in this section. Theoretical analyses used in this section mostly follow Sheppard and Wilson's excellent work in the 1990s.

When a pinhole is used in the confocal microscope detector, the detection is incoherent; thus, the axial intensity of the light is integrated over the area of the pinhole detector, such that:

$$I_i(z) = \int_{D_i} |E|^2 S_i dD_i \tag{3.27}$$

where D_i is the area and S_i is the sensitivity of the incoherent detector. The electric field is such that:

$$\begin{aligned} |E|^2 &= E_x E_x^* + E_y E_y^* + E_z E_z^* \\ &= |I_0|^2 + 2\Re(I_0 I_2^*)\cos\left[2(\gamma - \theta_p\right] + |I_2|^2 + 2|I_1|^2\cos^2(\gamma - \theta_p) \end{aligned} \tag{3.28}$$

where γ denotes the angle of incident polarization with respect to x-axis, θ_p is the angular component of the position vector, and $\Re$ represents real-part. I_0, I_1, and I_2 are intensity components with respect to the polarization vector, which are related to the electric field as such:

$$\begin{aligned} E_x &= -\frac{\kappa}{2}\left[\cos\gamma\left(I_0 + I_2\cos 2\theta_p\right) + \sin\gamma I_2 \sin 2\theta_p\right], \\ E_y &= -\frac{\kappa}{2}\left[\cos\gamma I_2 \sin 2\theta_p + \sin\gamma(I_0 - I_2\cos 2\theta_p)\right], \\ E_z &= -i\kappa\left[\cos\gamma I_1 \cos\theta_p + \sin\gamma I_1 \sin\theta_p\right] \end{aligned} \tag{3.29}$$

Using Eq. 3.27 in Eq. 3.28 for spherical coordinate, we obtain:

$$I_i(z) = \int_0^R \left(|I_0|^2 + 2|I_1|^2 + |I_2|^2\right)\rho d\rho \tag{3.30}$$

where R is the radius of the detector aperture.

For coherent detection using an optical fiber, the axial intensity is the integration over the field mode of the incident light which is given as:

$$I_c(z) = \left| \int_{D_c} ES_c dD_c \right|^2 \tag{3.31}$$

Since the terms of Eq. 3.29 consisting of $\sin\theta_p$, $\sin 2\theta_p$, $\cos\theta_p$, and $\cos 2\theta_p$ yield zero when D_c, Eq. 3.31 can be expressed as:

$$I_c(z) = \left| (\cos\gamma + \sin\gamma) \int_0^R I_0 \rho d\rho \right|^2 \tag{3.32}$$

Different from the incoherent detection of Eq. 3.30, the coherent detection shown in Eq. 3.32 exhibits explicit dependence on the polarization angle of the incident light, γ. When the radius of both the pinhole and the optical fiber core becomes point-like, the axial responses from both systems become identical.

3.2.4.2 Signal Collection

When the shot noise is the only source of the noise in the imaging system, then the signal-to-noise ratio (SNR) is given as [12]:

$$SNR = \frac{n_p}{\sqrt{n_p}} = \sqrt{n_p} \tag{3.33}$$

where the number of photons (n_p) is related to the incident power (P), wavelength (λ), incident time (t), Planck's constant (h), and speed of light (c), such that:

$$n_p = \frac{Pt\lambda}{hc} \tag{3.34}$$

For a detection system with quantum efficiency Q_E, SNR is given in terms of Q_E, n_p, and the number of involved electrons, n_n:

$$SNR = \frac{Q_E n_p}{\sqrt{Q_E n_p + n_n^2}} \tag{3.35}$$

SNR for a confocal microscope when assuming negligible electronic noise ($n_n = 0$) is given as:

$$SNR = \sqrt{Q_E n_p} \frac{F(v)}{\sqrt{F(v) + av^2/\sqrt{4}}} \tag{3.36}$$

where v is the normalized coordinate of Eq. 3.19, F(v) is the fraction of signal incident on the pinhole, and a is a constant representing the background noise

level. Background noise in majority of confocal microscopy systems is out-of-focus scattered light from thick specimen. For a circular pinhole and small v:

$$SNR = \sqrt{Q_E n_p}\frac{v}{2\sqrt{1+a}} \tag{3.37}$$

Equation 3.37 tells us that SNR increases as the pinhole diameter r, thus v, increases, and that as the background noise level—thus a—decreases.

In FOCM, SNR of the confocal microscopy expressed by Eq. 3.37 holds; however, the limited acceptance angle of the optical fiber reduces the signal level, which is one of the biggest differences from bulk confocal microscopy. This can be expressed by numerical aperture of optical fiber (NA_{fiber}). Normalized frequency, or V-number, of an optical fiber is given by:

$$V = \frac{2\pi r}{\lambda}\sqrt{n_1^2 - n_2^2} = \frac{2\pi r}{\lambda} NA_{fiber} \tag{3.38}$$

where r is the core radius, n_1 and n_2 are refractive indices of core and cladding, respectively. NA_{fiber} represents the numerical aperture of the fiber. Thus, for a given optical fiber and laser, confocality condition Eq. 3.26 can be re-written in terms of NA_{fiber}:

$$r = \frac{\lambda V}{2\pi NA_{fiber}} < \frac{\lambda}{4\pi n \sin\alpha} \tag{3.39}$$

After some arrangement, the requirement for the NA_{fiber} for confocal operation of a microscope becomes:

$$V 2n \sin\alpha < NA_{fiber} \tag{3.40}$$

This gives a good insight into how numerical apertures of the objective lens and the fiber play their role in confocal microscopy. V is a value smaller than 2.405 for single-mode operation of the fiber. Refractive index, n, is in general larger than 1. Thus, NA of the objective lens ($\sin\alpha = NA_{obj}$) must be much smaller than NA_{fiber}, or NA_{fiber} must be much larger than NA_{obj}. To achieve high efficiency of coupling light into an optical fiber, the focusing lens must provide high NA_{obj} so that the focused spot size can be comparable to the core size. High NA_{obj} may sacrifice confocality because of Eq. 3.40; thus, a compromise between coupling efficiency and confocality must be found. Lowered coupling efficiency causes lowered SNR. Since the detection fiber does not have to be operated in single-mode, a large-core high-NA optical fiber is more suitable for detection fiber, which gives both high coupling efficiency and confocality.

The same method used in Sect. 3.1.3 can be used to study the normalized coupling coefficient for different objective lenses in a single-fiber confocal setup. In this single-fiber confocal setup, an optical fiber is used for both illumination and detection. Assuming the profile of the input beam exiting from the fiber tip has a Gaussian distribution as before, the ray-transfer matrix can be calculated as [13]:

$$A = D = -\frac{f_2^2 - 2L_1f_2 + 2f_1f_2 - 2L_2f_2 + 2L_2L_1 - 2L_2f_1}{f_2^2}$$
$$B = -2\frac{f_1^2}{f_2^2}(f_2 - L_2) \tag{3.41}$$
$$C = -\frac{2(f_1 + f_2 - L_1)(f_1f_2 - L_1f_2 + L_2L_1 - L_2f_1 - L_2f_2)}{f_1^2f_2^2}$$

where f_1 and f_2 are the focal lengths of the two microscopic objective lenses, L_1 is the distance between the two lenses, and L_2 is the distance between the sample membrane and the f_2 lens (Fig. 3.20). Simplifications to the above expressions can be achieved if we assume $L_1 = f_1 + f_2$:

$$\mathrm{A} = \mathrm{D} = 1,\ \mathrm{C} = 0,\ \mathrm{B} = -2\frac{f_1^2}{f_2^2}(f_2 - L_2) \tag{3.42}$$

Because the input beam exiting from the fiber tip has a flat wavefront, q_1 can be written as:

$$\frac{1}{q_1} = \frac{1}{R_1} - i\frac{\lambda}{\pi w_0^2} = -i\frac{\lambda}{\pi w_0^2} \tag{3.43}$$

where w_0 and R_1 are the beam waist and the radius of curvature of the input Gaussian beam, respectively. By substituting Eqs. (3.42 and 3.43) into (3.40), the q-parameter of the return beam can be easily written as

$$q_2 = q_1 - 2\frac{f_1^2}{f_2^2}(f_2 - L_2) = i\frac{\pi w_0^2}{\lambda} - 2\frac{f_1^2}{f_2^2}(f_2 - L_2) \tag{3.44}$$

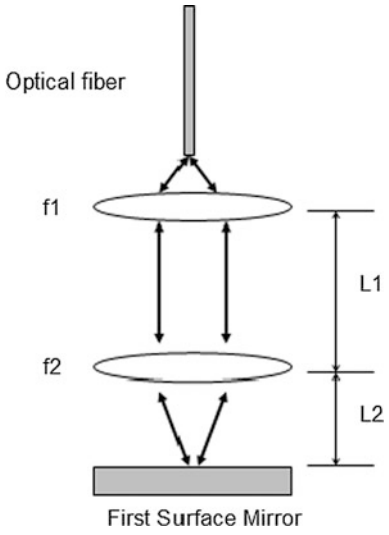

Fig. 3.20 Schematic of a single fiber confocal microscopy setup for studying power collection ratio

Since we also have

$$\frac{1}{q_2} = \frac{1}{R_2} - i\frac{\lambda}{\pi w_2^2} \tag{3.45}$$

by comparing the real and imaginary parts of Eq. (3.44) and (3.45), we can obtain the radius of curvature R_2 and the waist w_2 of the output beam, respectively:

$$R_2 = -\frac{(\frac{\pi w_0^2}{\lambda})^2 + 4(\frac{f_1}{f_2})^4 (f_2 - L_2)^2}{2\frac{f_1^2}{f_2^2}(f_2 - L_2)} \tag{3.46}$$

$$w_2^2 = (\frac{\lambda}{\pi w_0})^2 \left[(\frac{\pi w_0^2}{\lambda})^2 + 4(\frac{f_1}{f_2})^4 (f_2 - L_2)^2 \right] \tag{3.47}$$

The optical power collected by the fiber tip is the integral of the beam intensity over the fiber core area at the fiber tip plane, as was the case in Eqs. 3.9, and 3.10 can be used to calculate T, which shows the confocal effect of the system.

3.2.4.3 Variations of FOCM

The FOCM arrangement shown in Fig. 3.21 is a setup which utilizes the advantage of using optical fiber as a point-like light source and as a point coherent detector. The FOCM of Fig. 3.21 is especially useful in establishing a cost-effective confocal microscopy system because a low-cost diode laser can be used, and other optical components such as beam-splitter and pinholes can be avoided. However, it does not utilize the advantage of optical fiber in terms of flexibility and robustness, which enables compact remote sensing. Beam scanning at the distal end of the optical fiber needs a special design.

One of the commonly used arrangements of compact remote sensing FOCM is shown in Fig. 3.22. The bulk scanning optics of the arrangement in Fig. 3.21 were replaced with a miniature endoscopic fiber scanner. The micro actuator translates the fiber tip, which serves the role of a point-like light source and point detector at the same time in a raster or spiral scanning pattern in a small package. The descanned detector through the scanning fiber tip ensures confocal operation of the system. The objective lens can be a common spherical lens or graded index (GRIN) lens. The entire scanning section can be sealed in a compact package; thus, this arrangement is suitable for endoscopic application. However, mechanical scanning of the fiber tip in a small endoscopic package may limit the size of the entire package.

Another method for compact remote scanning is shown in Fig. 3.23 [14]. This arrangement uses an optical fiber bundle to deliver the scanning light signal from and to the scanning microscope. The scanning microscope does not have to operate under a confocal regime, but it has to be able to deliver an illumination laser into a single core of the fiber bundle while detecting a signal from the same core. Optical

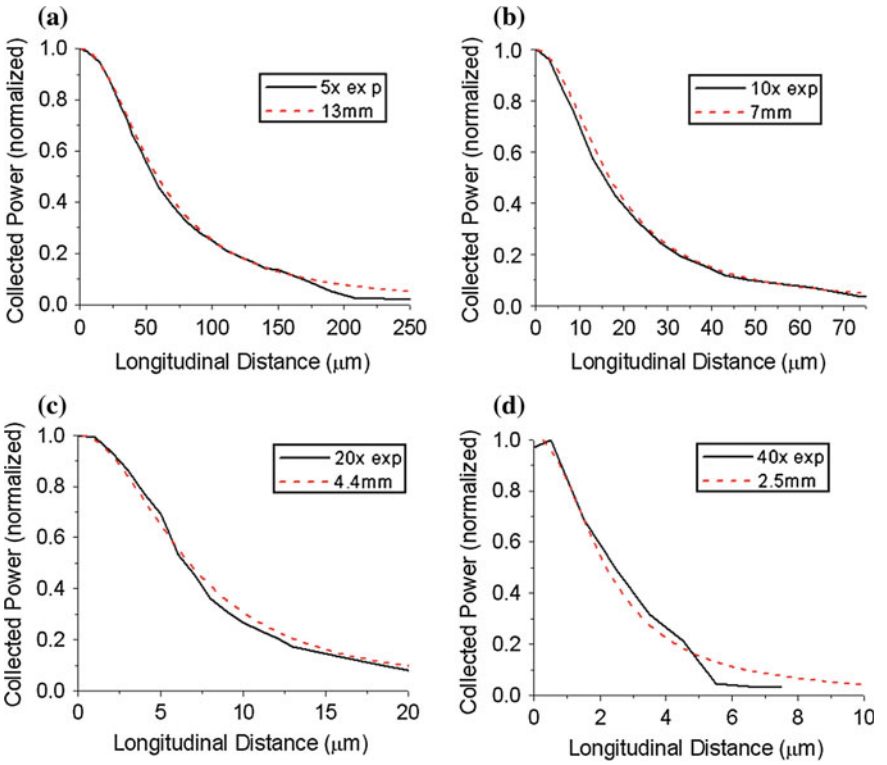

Fig. 3.21 Experimental (*solid*) and simulation (*dashed*) results showing the fiber optic confocal effect for four different microscopic objective lenses. The measured FWHM of the longitudinal confocal response was found to be (*a*) 5X: 102 μm, (*b*) 10X: 28.4 μm, (*c*) 20X: 11 μm, and (*d*) 40X: 4.4 μm, respectively

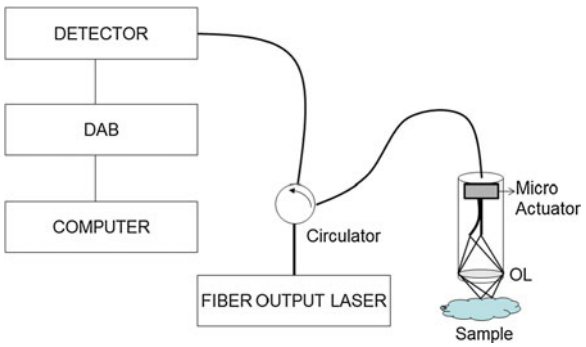

Fig. 3.22 FOCM with scanning implemented on the distal end of the optical fiber. The micro actuator introduces raster or spiral scanning of the fiber-tip. OL represents the objective lens

arrangement of the fiber bundle and objective lens should be such that the detection is achieved in high confocality. Using a GRIN lens will further minimize the size of the setup.

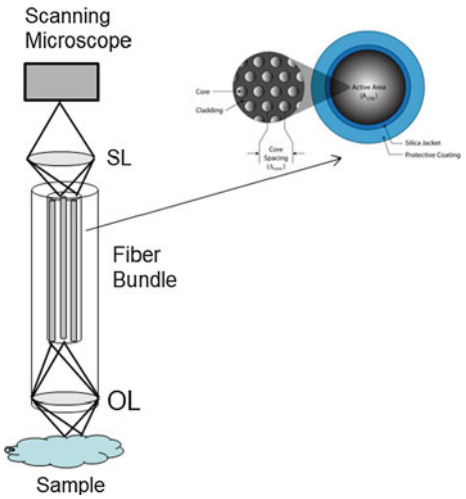

Fig. 3.23 Endoscopic FOCM based on fiber bundle. Inset shows the multiple core structure of the fiber bundle

3.3 Novel Application of FOCM

Confocal microscopy has been widely used in many practical fields ranging from basic science to industrial applications due to its depth discrimination property, which can be utilized for three-dimensional imaging of thick specimens [15–17]. The disadvantages of conventional pinholes used in normal confocal microscopes have been overcome by replacing the pinholes with optical fiber [11], resulting in the achievement of higher resolution [18]. Hollow-core fibers have been developed since the surgical application of mid-infrared (IR) lasers was established. However, typical hollow-core fibers have been made of metal-coated or dielectric-coated quartz or plastic tubes, and they have larger than a few hundred micrometers of diameter due to technical difficulties of production. Mid-IR applications and hollow-core fiber deliveries are well summarized in many chapters

Yablonovitch was the first to propose that the periodicity in dielectric materials could prevent the propagation of electromagnetic waves within a certain frequency range. The periodicity of the dielectric constant induces the removal of degeneracy of the free-photon states at Bragg planes and provokes a range of forbidden energies for the photons. This has led to the appearance of a photonic crystal also known as photonic bandgap material. There is a close analogy between electrons in semiconductors and photons in photonic crystals. Many concepts valid for electrons can now be extended to photons.

From the Maxwell's equations, we can eliminate the electric field E(r) and write the wave equation in terms of the magnetic field H(r):

$$\nabla \times \left(\frac{1}{\varepsilon(r)} \nabla \times H(r) \right) = \frac{\omega^2}{c^2} H(r) \tag{3.48}$$

And the transverse requirement needs to be satisfied:

$$\nabla \cdot H(r) = 0 \tag{3.49}$$

This is an eigenvalue problem. For a specific structure, ε(r) and H(r) are solved for some frequency. The electric field can be calculated by the following relation:

$$E(r) = \left(\frac{-i}{\omega\varepsilon(r)}\right)\nabla \times H(r) \tag{3.50}$$

Let us consider a one-dimensional (1-D) structure as shown in Fig. 3.24, which is constituted of an array of alternating dielectric materials with dielectric constants n_1 and n_2, and a period of a. From Bloch's theorem, the eigenstates of the translation operator in x direction, which are plane wave $e^{ik_x x}$, are also the eigenstates of the wavefunction Eq. (3.48). Thus the one-dimensional eigenstate of magnetic field can be expressed as:

$$H_k(x) = e^{ik_x x}u_k(x) \tag{3.51}$$

After a somewhat complex mathematical procedure, applying Eq. (3.51) into Eq. (3.48) leads to:

$$\Theta_k u_k(x) = \left(\frac{\omega(k)}{c}\right)^2 u_k(x) \tag{3.52}$$

where Θ_k is a Hermitian differential operator defined as

$$\Theta_k = (ik_x + \partial x) \times \left(\frac{1}{\varepsilon(x)}(ik_x + \partial x)\times\right) \tag{3.53}$$

We find from Eqs. (3.52) and (3.53) a very familiar structure of quantum physics: a Hamiltonian eigenvalue problem. Using the analogy of quantum physics, we can induce a dielectric version of Bloch's theorem

$$u_k(x) = u_k(x + a) \tag{3.54}$$

from which the dielectric version of the Brillouin zone is also predictable. Omitting all the details of quantum physics analogy, two conclusions can be made: (1) For an infinite periodic structure similar to Fig. 3.24, all the eigenfunctions can be expressed in terms of the eigenfunction of the first Brillouin zone (any one pair of n_1 and n_2 in Fig. 3.24); (2) Angular frequency ω(k) which appears in Eq. (3.52)

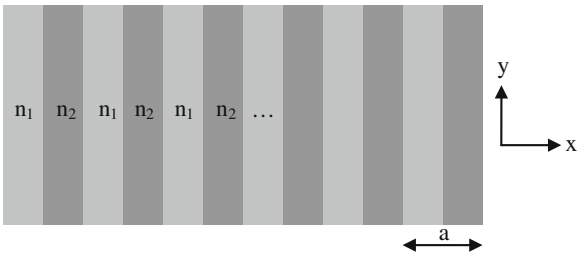

Fig. 3.24 One-dimensional periodic array of dielectric material with refractive index n_1 and n_2

can have only values satisfying the dispersion relation (solid line), which is graphically expressed in Fig. 3.25.

Figure 3.25 shows that some range of frequency values are not allowed for a certain value of wave vectors, which is marked as the shaded area named photonic bandgap. That is to say, in a periodic dielectric structure, light having a certain frequency (wavelength) cannot exist. By placing different photonic bandgap materials in a well-planned manner, a photonic well—an analogy of a quantum well in quantum physics—can be constructed and light can be confined only in a desired region. Extension of the above periodic 1-D structure to x–y plane, and placing the same structure along z-axis, a new type of light-guiding structure can be constructed–a photonic bandgap (or photonic crystal) fiber [19]. Photonic bandgap fibers have such versatility that virtually any size or shape of any wavelength of light-guiding core can be obtained by proper design of the bandgap structure and usage of bandgap materials. Photonic crystal fibers have recently been developed in various structures and have theoretically and experimentally been shown to have several advantages over conventional silica-based fibers, e.g., low temperature dependence [20], hollow-core mid-IR guidance [21]. Our main interest is to utilize hollow-core photonic bandgap fiber in single-fiber confocal microscopy, which can lead to real-time imaging while delivering mid-IR surgical laser power in the same single fiber.

A confocal microscope using a single optical fiber was built as shown in Fig. 3.26 [22]. A 532 nm solid state laser and Crystal Fiber's HC-530-01 hollow-core photonic bandgap fiber (HC-PBF, core diameter: 5 μm, center wavelength: 511 nm) were used for the experimental setup; however, other lasers and fibers—such as 632.8 nm He–Ne laser and gold-coated hollow-core fiber (HCF, core diameter 700 nm)—were also used for comparison. To obtain optimum results, we tried different objective lenses for coupling, collimating, and focusing (OL1-OL3),

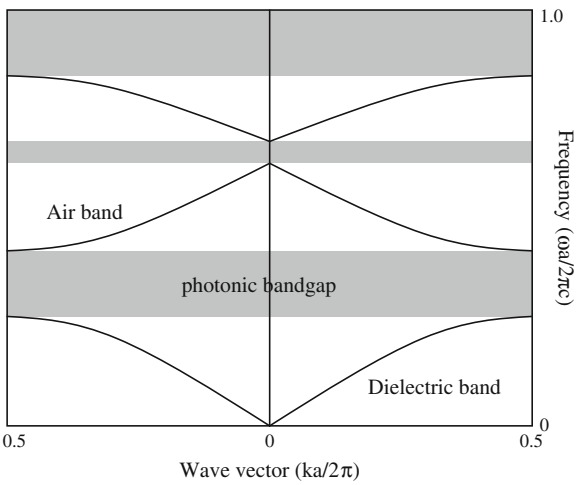

Fig. 3.25 Dispersion relation of 1-D photonic bandgap material in the first Brillouin zone

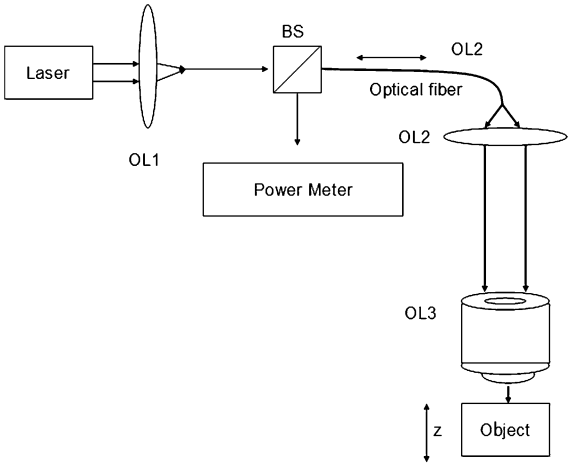

Fig. 3.26 Schematic of experimental setup. *BS* beamsplitter, *OL1* coupling lens, *OL2* collimating lens, *OL3* confocal lens, z defocusing displacement of a reflective object

ranging from 5× to 100×. The structure of the HC-PBF used for the experiment is shown in Fig. 3.27.

The axial response was measured and the experimental results with HC-PBF and 10×, 20×, and 60× focusing lenses are shown in Fig. 3.28. A solid state laser with a wavelength of 532 nm, an output power of 25 mW, and a beam diameter of 0.7 mm was used along with a beamsplitting cube. A dielectric total-reflection mirror was used as the object. The output power was in the microwatt range revealing very low coupling efficiency, which was mainly due to the transmission loss from the particular HC-PBF sample we used for the experiment.

The factory-specified transmission loss is <1 dB/m; however, the unit used has > 3 dB/m loss. FWHM were 14.7, 6.9, and 2.1 μm for the 10×, 20×, and 60× OL3's, respectively. Using the values of NA of the objective lenses as summarized in Table 3.2, the ratio of FWHM for confocal systems using 10×, 20×, and 60× lenses is 16:6.25:1.38, which is in close agreement with the ratio of the experimental data, 14.7:6.9:2.1, within experimental errors.

Figure 3.29 shows the experimental results with HCF and He–Ne laser with a wavelength of 632.8 nm, output power of 18.5 mW, and beam diameter of 1.8 mm which was used along with a beamsplitting cube.

As we expected from a larger core diameter, the confocal signal showed intensity as high as 2 mW. FWHM were 55 and 16 μm for 40× and 60×, respectively. Results from HCF showed a relatively large depth resolution, which is not suitable for high-resolution confocal microscopy; however, we expect normalized defocus ($\sim z/\lambda$) remains the same when defocusing displacement (z) and wavelength (λ) increase simultaneously, leaving the shape (i.e., FWHM) of the output signal the same.

Another advantage of confocal microscopy using hollow-core fiber is very a low Fresnel back-reflection at the air-fiber interface. We could not fully utilize this advantage at this time due to the fact that fiber couplers made with hollow-core or

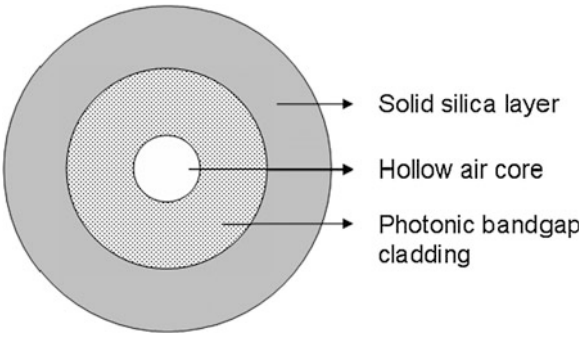

Fig. 3.27 Schematic of cross-section of HC-PBF

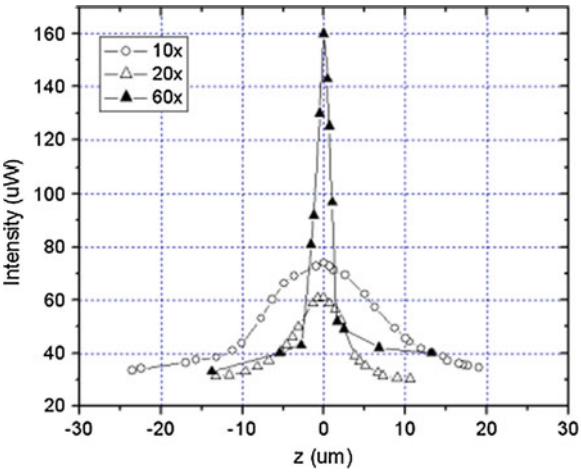

Fig. 3.28 Experimental axial responses obtained with 1 m of HC-PBF, OL1 = 20×, OL2 = 10×, and different OL3's marked as legends in the graph

Table 3.2 Specifications of objective lenses used for the experiment

	NNA	Focal length, f (mm)	WD (mm)
5×	0.10	25.4	13.0
10×	0.25	16.5	5.5
20×	0.40	9.0	1.7
40×	0.65	4.5	0.6
60×	0.85	2.9	0.3

photonic bandgap fibers have not been developed yet; thus, a single fiber configuration using a beamsplitting cube—another source of signal decrease from back-reflection—was adapted. Total back-reflection through the system was measured at 30 μW when HC-PBF was used and 200 μW when a solid-core single-mode fiber was used. That is an 85 % reduction of background level obtainable without anti-reflection coating or angle cleaving of the fiber tips. To reduce the back-reflection at the surfaces of the beamsplitting cube, we

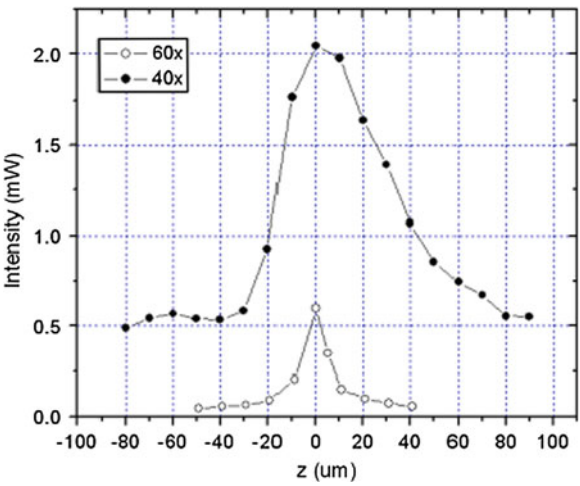

Fig. 3.29 Experimental axial responses obtained with 1 m of HCF, OL1 = 5×, OL2 = 10×, and OL3 was 40× and 60×

investigated a mirror with a hole. A small hole with diameter d1 was drilled in 45 degree through the mirror, where d_1 is the beam diameter of the laser (Fig. 3.30).

When the confocal signal coming out from the fiber is collimated through the lens, OL1, it will have a larger diameter than the input laser according to the NA of fiber and working distance of OL1. For a fixed value of NA of a fiber, the larger the WD, the larger the signal reflected at the mirror back into the power meter. For a fixed d1 and a given OL1, however, a larger WD means a longer focal length, which will result in a larger spot size (d_3) of the input laser at the fiber tip and will lead to poor coupling efficiency. Using a 532 nm solid state laser with $d_1 = 0.7$ mm, the focused spot size was calculated using the formula $w = 4\lambda f/(3\pi w_0)$ to be 21.3, 11.6, and 3.74 μm for 10×, 20×, 60× lenses, respectively.

Although the spot size is larger than the core diameter (d_0) of HC-PBF, 20× showed the best input coupling due to a smaller NA of 0.40 than that of 60× lens. The beam-splitting efficiency, $\eta_1 = (1 - d_1^2/d_2^2)$, was not physically meaningful for 20× as d_2 is smaller than d_1. Note that d_2 can be calculated from the relation, $d_2 = 2WD\tan\alpha$. The proper choice of d1 and OL1 is needed for a given wavelength and fiber for better total efficiency. Assuming a simple coupling efficiency as $\eta_2 = d_0^2/d_3^2$, total efficiency ($\eta_1 \times \eta_2$) was calculated and plotted in Fig. 3.31 for different lasers, (a) for 5 μm core fiber and (b) for 8 μm core fiber.

The optimal result is predicted from the calculation to be when a lens with f = 4 mm (40×) was used in corporation with solid state laser, or when a lens with f = 7.5 mm (20×) was used with He–Ne leaser; however, $d_2 < d_1$ for both lenses, thus 10× lens was used for the measurement. The background level was as low as 15 μW compared to 30 μW when a beam-splitting cube was used. Figure 3.31b when compared to Fig. 3.31a shows that the efficiency can be improved when a fiber with a larger core diameter is used. Note that most of mid-IR hollow-core fibers have >50 μm core diameter.

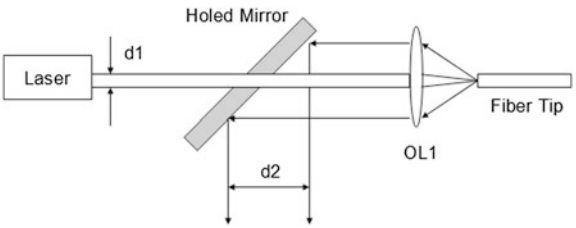

Fig. 3.30 Detailed schematic of the beam-splitting section using a mirror with a hole. *WD* working distance of OL1, d_1 diameter of laser beam, d_2 diameter of collimated output

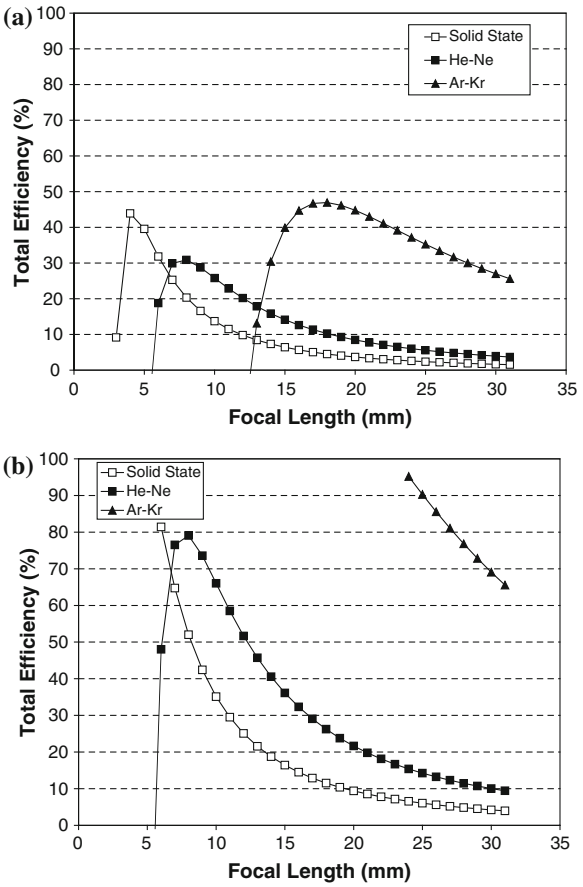

Fig. 3.31 Theoretical calculation of total detection efficiency for different lasers. Beam diameter is 0.7, 1.3, 3.0 mm, and the wavelength is 532, 632.8, 514.5 nm for the solid state laser, He–Ne laser, Ar-Kr laser, respectively. The fiber is set to have core diameter of **a** 5 μm and **b** 8 μm. NA is assumed to be 0.12 for both cases

Figure 3.32 shows the experimental results of the axial resolution measurement using the designed holed-mirror type of beamsplitter. There is a hole with a 0.7 mm diameter, at an angle of 45 degrees to the mirror surface and the input laser passes through the hole before being coupled to the HC-PBF. For precise measurement of the axial resolution, a nano-positioning piezo-electric translational

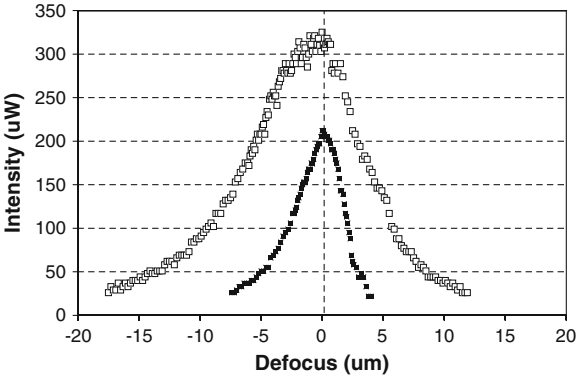

Fig. 3.32 Experimental axial responses obtained with 50 cm of HC-PBF, OL1 = 10×, OL2 = 10×. OL3 was 60× for solid squares and 40× for open squares

stage was used to move the object. The precision of the movement is as low as ~100 nm. The actual movement step used for the experiment was 200 nm. Using 50 cm of HC-PBF, OL1 = 10×, OL2 = 10×, FWHM was measured to be 4.70 μm for 60× OL3, and 10.4 μm for 40× OL3. Reduction of the background level by usage of a holed-mirror beamsplitter was 50 % lower than that of a cubic beamsplitter.

References

1. Mertz J (2009) Introduction to optical microscopy. Roberts and Company publishers, Colorado
2. Pawley JB (ed) (1995) Handbook of biological confocal microscopy. Plenum Press, New York
3. Slayter EM, Slayter HS (1992) Light and electron microscopy. Cambridge University Perss, Cambridge
. Born M, Wolf E (1999) Principles of optics, 7th edn. Cambridge University Press, Cambridge
5. Minsky M (1961) US Patent 3,013,467
6. Wilson T, Sheppard CJR (1984) Theory and practice of scanning optical microscopy. Academic Press, London
7. Lukosz W (1996) Optical systems with resolving powers exceeding classical limit, j. Opt. Soc Am 56:1463
8. Wilson T, Carlini AR (1987) Size of the detector in confocal imaging systems. Opt Lett 12(4):227–229
9. Nakano A (2002) Spinning-disk confocal microscopy: a cutting-edge tool for imaging of membrane traffic. Cell Structure and Function 27(5):349–355
10. Verveer PJ, Hanley QS, Verbeek PW, Van Vliet LJ, Jovin TM (1998) Theory of confocal fluorescence imaging in the programmable array microscope. J Microscopy 189:192–198
11. Dabbs TP, Glass M (1992) Fiber-optic confocal microscope: FOCON. Appl Opt 31:3030–3035
12. Sheppard CJR, Gu M, Roy M (1992) Signal-to-noise ratio in confocal microscope systems. J Microsc 168:209–218
13. Sharma U, Chen G, Kang JU, Ilev I, Waynant RW (2005) Fiber optic confocal laser Doppler velocimeter using an all-fiber laser source for high resolution measurements. Opt Expr 13(16):6250–6258

14. Lee CM, Engelbrecht CJ, Soper TD, Helmchen F, Seibel EJ (2010) Scanning fiber endoscopy with highly flexible 1mm catheterscopes for wide-field, full-color imaging. J Biophotonics 3(5–6):385–407
15. Carlsson K, Aslund N (1987) Confocal imaging for 3-D digital microscopy. Appl Opt 26:3232–3238
16. Hamilton DK, Wilson T (1982) Surface profile measurement using the confocal microscope. J Appl Phys 53:5320–5322
17. Wilson T (1990) Confocal microscopy academic. San Diego, Calif
18. Bae JH, Kim KH, Hong MH, Gim CH, Jhe W (2000) High-resolution confocal detection of nanometric displacement by use of a 2 × 1 optical fiber coupler. Opt Lett 25:1696–1698
19. Knight JC (2003) Photonic crystal fibers. Nature 424:847–851
20. Kim DH, Kang JU (2004) Sagnac loop interferometer based on polarization maintaining photonic crystal fiber with reduced temperature sensitivity. Opt Express 12:4490–4495
21. Shephard JD, MacPherson WN, Maier RRJ, Jones JDC, Hand DP, Mohebbi M, George AK, Roberts PJ, Knight JC (2005) Single-mode mid-IR guidance in a hollow-core photonic crystal fiber. Opt Expr 13:7139–7144
22. Kim DH, Kang JU, Ilev IK (2007) An advanced confocal microscope using a single hollow-core photonic bandgap fiber design. Electonic Letters 43(11):608–609